# Effects of heat treatment on the microstructure characteristics and mechanical performance of vacuum-assisted die-casting Al80Si8Mg4Cu4Zn4 alloys

# Wen-hui Bai, \*Hai-dong Zhao, Su-ya Feng, Wu-qiang Zhu

National Engineering Research Center of Near-net-shape Forming for Metallic Materials, South China University of Technology, Guangzhou 510640, China

 $*Corresponding \ address: e-mail: zhaohaidong@tsinghua.org.cn, hdzhao@scut.edu.cn.\\$ 

Abstract: The strength-plasticity trade-off in Al-based entropy alloys (Al-EAs) remains challenging. In this work, a new Al-EA was designed by a calculated phase diagram (CALPHAD) framework and thermodynamic parameters. The alloy was produced using the industrial vacuum-assisted die casting. The alloy smicrostructural evolution and mechanical performance under heat treatment were characterized across room-temperature and high-temperature regimes. After heat treatment, Numerous  $\beta''$ ,  $\theta''$ , and  $\eta''$  phases precipitated, maintaining full or semi-coherent interfaces with the Al matrix, resulting in precipitation strengthening. High concentrations of stacking faults and twins, along with nano-scale Al2Cu phases, further strengthen the alloy. The Al2Cu phase network was substantially reduced (from 88.32% to 27.69%), while the Q phase exhibited minimal changes in connectivity. The heat treatment process enhances the alloy's strength at room temperature; however, it leads to a degradation in high-temperature strength. After solution treatment at 450 ° C for 1 h and subsequent aging at 70 ° C for 24 h (denoted as the 450 ° C-1 h alloy), the alloy demonstrates enhanced tensile and compressive properties at room temperature. With enhanced plasticity, the alloy achieves 376 MPa in tensile strength and 919 MPa in compressive strength. Whereas, the as-cast alloy shows improved strength at elevated temperatures, mainly attributed to the highly interconnected network of intermetallic compounds (IMCs).

**Keywords:** Al-based entropy alloys; Vacuum-assisted die casting; Heat treatment; Microstructure; Mechanical performance.

# 1 Introduction

alloys Aluminum (Al) have emerged indispensable materials in modern industry, owing to their exceptional combination of lightweight properties, superior strength-to-weight ratio, corrosion resistance, and superior machinability [1, 2]. With the growth of the green economy, there is an increasing demand for high-strength, lightweight Al alloys. However, the conventional alloy design approach has been highly limited in exploring the full spectrum of potential alloys [3], because the central area of a multicomponent phase diagram encompasses a vastly greater number of possible compositions compared to the corner regions [4].

High-entropy alloys (HEAs), refer to multicomponent alloys with five or more components and high configurational entropy, have attracted considerable interest owing to their outstanding mechanical performance <sup>[5, 6]</sup>. Lightweight HEAs are made up of light elements, including Al, Mg, Ti, Li, and Be <sup>[7]</sup>. Compared to refractory HEAs, lightweight HEAs

offer reduced density while retaining high strength, superior corrosion resistance, and favorable thermal stability [8,9]. To achieve a further reduction in density, an increasing number of lightweight main-group elements are being incorporated [10]. A newly emerging category of alloys, known as Al-based entropy alloys (Al-EAs), has garnered significant interest [11-13]. For instance, Wen et al. [14] manufactured a novel Al<sub>70</sub>Zn<sub>10</sub>Mg<sub>10</sub>Cu<sub>5</sub>Si<sub>5</sub> alloy through electromagnetic stirring and homogenization treatment. The ultimate compressive strength and compressive yield strength were measured at 497 MPa and 432 MPa, respectively, with an observed fracture strain of about 10%. In addition, Beak et al. [15] investigated the effects of ultrasonic melt treatment and solution treatment on the microstructure and mechanical properties of the Al<sub>70</sub>Mg<sub>10</sub>Si<sub>10</sub>Cu<sub>5</sub>Zn<sub>5</sub> multicomponent alloy, which exhibited high strength at temperatures below 200°C. Studies on lightweight Al-EAs indicate that the high-entropy design strategy can effectively enhance strength-plasticity synergy.

The primary melting techniques used for producing HEAs include vacuum arc melting and vacuum induction [16]. However, excessive solute content melting significantly increases melt viscosity and deteriorates casting properties. In large-scale ingots, this unavoidably causes severe imperfections such as compositional segregation and shrinkage cavities [17]. Cast Al-Si alloys are the most widely used aluminum casting alloys owing to their superior castability, excellent wear resistance, balanced mechanical properties, and strong corrosion resistance [18], which are extensively applied in the automotive, aerospace, marine, and electronics industries [19]. Unfortunately, research on Al-EAs designed based on Al-Si system is very limited.

High-pressure die casting (HPDC) is an efficient and high-precision manufacturing process commonly employed for producing lightweight metal components, including Al, magnesium (Mg), and zinc (Zn) alloys [20, 21]. Vacuum-assisted die casting is a high-tech die casting method that evacuates air from the mold cavity under high vacuum conditions. This minimizes gas porosity, resulting in denser castings with superior mechanical properties [22]. The process is being extended to large-and giga castings, including rear floor components in numerous electric vehicles [23] Furthermore, various heat treatment methods can improve the mechanical properties of the castings without inducing blister formation. Regrettably, there has been very little research on die-casting Al-EAs.

To explore the potential of Al-EAs with better mechanical performance, a new Al-EA (Al<sub>80</sub>Si<sub>8</sub>Mg<sub>4</sub>Cu<sub>4</sub>Zn<sub>4</sub>) was designed and investigated in this study. The elemental ratios were adjusted to optimize key empirical thermodynamic parameters, including mixing entropy, enthalpy, and others. Additionally, Thermo-Calc simulations were used to predict the phase composition. The alloys were fabricated using industrial-scale die casting. A systematic investigation was conducted on their phase formation, microstructure, and mechanical properties under various heat treatment conditions. In addition, the correlation between microstructure and mechanical performance was further investigated.

# 2 Experimental sections

In this study, the alloys were prepared using industrial pure Al (99.85wt.%), pure Zn (99.9wt.%), Al-20Si, Al-50Mg, and Al-50Cu master alloys. Prior to melting, all alloy materials were preheated to 200°C to eliminate any residual moisture. First, industrial pure Al,

Al-20Si, and Al-50Cu master alloys were placed in a graphite crucible and melted at 720°C using an electric resistance furnace. Following 30 min of homogenization, preheated pure Zn and Al-50Mg master alloys were introduced into the melt and held for another 30 min. The melt was then degassed by bubbling pure argons through it for 10 min. The melt temperature was lower to 650°C for the die casting process. The mechanical test specimens were produced using a TOYO BD-250 V5 cold-chamber die casting machine equipped with a high vacuum system. The mold temperature was maintained at 200°C, and an intensification pressure of 95 MPa was applied. The chemical compositions of the experimental alloys were analyzed using Inductively Coupled Plasma (ICP), and the results are presented in Table 1.

The die-casting alloys, after undergoing natural cooling at ambient temperature for a minimum of 24 h, were subjected to sequential solution treatment and artificially aging processes. Then, the alloys underwent solution heat treatment at 450°C in an electric resistance furnace, with durations of 0.5, 1, 2, and 3 h. Following solution treatment, the castings were water-quenched at 25°C and aged at 70°C for 24 h. For ease of description, the alloys solution treated at 450°C for 0.5, 1, 2, and 3 h were respectively labeled as 450°C-0.5h, 450°C-1h, 450°C-2h, and 450°C-3h alloys.

The equilibrium and non-equilibrium solidification calculations as a function of temperature were performed using Thermo-Calc (v. 2020a, Thermo-Calc Software AB, Stockholm, Sweden) in combination with the TCAL5 thermodynamic database. The Scheil-Gulliver model was employed to predict phase evolution under non-equilibrium solidification conditions.

The specimens for microstructure analysis were cut and prepared using standard metallographic techniques. The microstructures of the alloys were examined using optical microscopy (OM, LEICA DMI3000M) and scanning electron microscopy (SEM, Zeiss Sigma 300) coupled with energy-dispersive X-ray spectroscopy (EDS). The phases present in the alloys were determined using SEM-EDS. Transmission electron microscopy (TEM, Talos F200X) was employed to characterize the nano-scale precipitates, operating at an accelerating voltage of 200 kV. The TEM specimens were prepared via focused ion beam (FIB) milling using a JEOL JIB-4601F system. To characterize the multiscale microstructure and its temporal evolution in the alloys, a Zeiss Sigma 300VP FE-SEM integrated with a Gatan 3View ultramicrotome system was employed for serial

block-face scanning electron microscopy (SBFSEM). To minimize artifacts and enhance Z-axis (cutting direction) resolution, 3D image acquisition was performed at a cutting speed of 0.2 mm/s with a slice thickness of 30 nm [24]

Tensile and compression tests were conducted at room temperature using an electromechanical universal testing machine (MTS E44.304) with a 30 kN load cell, at a constant strain rate of  $1.0 \times 10^{-3}$  s<sup>-1</sup>. For compression tests, cylindrical specimens measuring 3 mm in diameter and 6 mm in length were employed. For tensile tests, dog-bone-shaped specimens were fabricated wire-electrode cutting, with gauge dimensions of 16 mm (length)  $\times$  3 mm (width)  $\times$  1.5 mm (thickness). To improve the accuracy, tensile and compression properties were averaged from at least three tests for each sample. The sampling locations are illustrated in Fig. 1(a), while the dimensions of the tensile and compression test specimens are provided in Fig. 1(b) and (c), respectively.

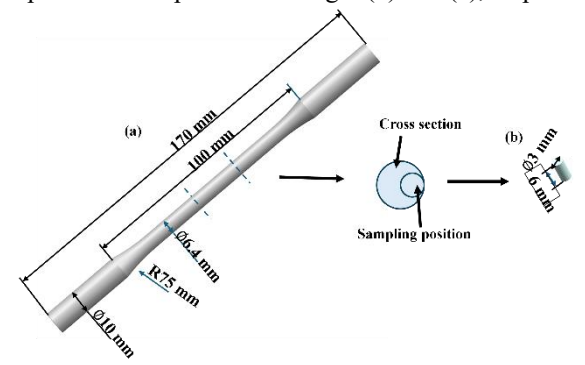


Fig.1: Geometry and size of: (a) tensile specimen and (b) compression specimen.

Table 1. Actual chemical composition and density (at.%) of experimental alloy.

	Si	Mg	Cu	Zn	Al
Nominal	8	4	4	4	80
Experimental	8.36	4.06	3.97	4.24	79.36

# 3 Results and discussion

# 3.1 Microstructure and phase constitution of Al<sub>80</sub>Si<sub>8</sub>Mg<sub>4</sub>Cu<sub>4</sub>Zn<sub>4</sub> alloy

Fig.2 shows the equilibrium and non-equilibrium phase diagram of the designed alloy. As illustrated in Fig.2(a), the alloy is anticipated to be multiphase, primarily consisting of a dominant  $\alpha$ -Al solid solution (FCC\_L2) strengthened by various intermetallic compounds (IMCs). The  $\alpha$ -Al is the main phase with a mole percentage of 72%. The  $\alpha$ -Al phase precipitates

first at the liquidus temperature (554°C). The Mg<sub>2</sub>Si (Mg<sub>2</sub>Si\_C1) and Si (Diamond\_A4) phases precipitate at 527°C. During solidification, the Mg<sub>2</sub>Si phase further transforms into the Q-phase (Q-ALCUMGSI). As solidification continues, the post-dendritic Al<sub>2</sub>Cu (Al2CU\_C16) phase precipitates from the supersaturated liquid. The solidus temperature occurs at 474°C. Furthermore, the phase diagram indicates the reversion of a Zn-rich phase from the  $\alpha$ -Al matrix at temperatures under 230°C.

The non-equilibrium phase diagram calculated using the Scheil-Gulliver model is presented in Fig. 2(b). Same as the equilibrium phase diagram, the α-Al phase precipitates firstly from the liquid at 554°C. In addition, the precipitation sequences of IMCs are consistent with the equilibrium solidification. However, the Mg<sub>2</sub>Si phase is stable up to room temperature and the solidification finishes at 340°C, which are different from the equilibrium solidification. It should be noted that the Scheil model assumes that the solid phase composition remains completely "frozen" (no diffusion) during solidification, leading to excessive solute enrichment in the last solidifying liquid phase and lowering the final solidification temperature. Moreover, as the solid mole fraction nears 1.0, a minimal amount of BCC B2, C14 LAVES, and HCP A3 phases precipitate from the remaining liquid, which are absent in equilibrium solidification.

Various thermodynamic and physical parameters have been introduced to predict the formation of solid solutions in HEAs  $^{[25,\ 26]}$ . In this study, the entropy of mixing (  $\Delta S_{mix}$  ), enthalpy of mixing (  $\Delta H_{mix}$  ), ratio between the  $\Delta H_{mix}$  and  $\Delta S_{mix}$  (  $\Omega$  ), atomic size difference ( $\delta$ ), and electronegativity ( $\Delta\chi$ ) were calculated as follows:

$$\Delta S_{mix} = -R \sum_{i=1}^{n} (c_i \ln c_i)$$
 (1)

$$\Delta H_{mix} = \sum_{i=1, i \neq j}^{n} 4\Delta H_{ij} c_i c_j$$
 (2)

$$\Omega = \frac{T_m \Delta S_{mix}}{|\Delta H_{mix}|} \tag{3}$$

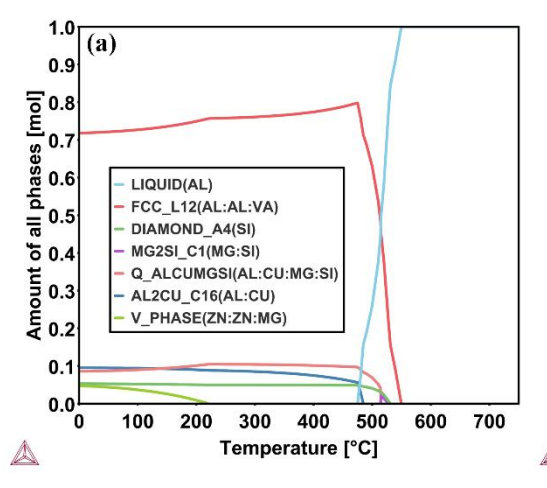
$$\delta = \sqrt{\sum_{i=1}^{n} c_i \left(1 - \frac{r_i}{\overline{r}}\right)^2} \cdot 100\% \tag{4}$$

$$\Delta \chi = \sqrt{\sum_{i=1}^{n} c_i (\chi_i - \overline{\chi})^2}$$
 (5)

where R denotes the gas constant,  $c_i$  and  $c_j$  represent the atomic percentages of the i-th and j-th elements, respectively;  $\Delta H_{mix}$  represents the mixing enthalpy between the ith and jth elements, computed using Miedema's model;  $T_m$  represents the average melting temperature of the alloy's constituent elements;  $r_i$  represents the atomic radius of the i-th element, while  $\overline{r}$  denotes the mean atomic radius across all elements.  $\chi_i$  is the Pauling electronegativity of component i, and  $\overline{\chi}$  is the average electronegativity across all constituent elements, weighted by composition. Table 2 lists the thermodynamic parameters of  $A_{80}Si_8Mg_4Cu_4Si_4$  alloy, as calculated by the empirical

formulas above.

Entropy alloys are categorized into HEAs, medium entropy alloys (MEAs), or low entropy alloys (LEAs) based on their configurational entropy: HEAs have values exceeding 1.5 R, MEAs range between 1 R and 1.5 R, and LEAs fall below 1 R. With entropy value of 6.38 J/mol·k (0.767 R), the experimental alloy falls into the low-entropy category. Nonetheless, its entropy level continues to be substantially greater than that of conventional Al alloys. Studies indicate that a single solid solution phase forms when  $\Omega \geq 1.1$  and  $\delta \leq 6.6\%$  [25]. The  $\Omega$  and  $\delta$  value of the experimental alloy is 1.1 and 6.04%, respectively, implying a simple phase formation. In addition, the  $\Delta \chi$  values are within the acceptable limit ( $\Delta \chi < 0.175$ ), ensuring solid solution stability in HEAs [27].



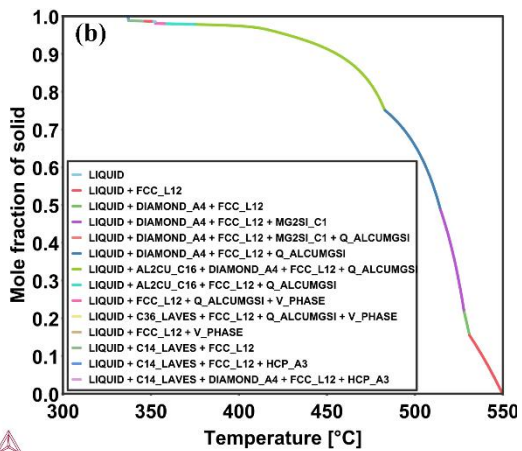


Fig.2: (a) The mole fraction of all phases versus temperature calculated by equilibrium solidification; (b) non-equilibrium phase diagrams obtained by Scheil-Gulliver model.

Table 2. The calculated thermodynamic parameters of the experimental alloy

Alloy	δ (%)	$\Delta H_{\text{mix}}$ (KJ/mol)	$\Delta S_{\text{mix}}$ (J/mol·K)	Ω	Δχ
$Al_{80}Si_8Mg_4Cu_4Zn_4$	6.04	-5.81	6.38	1.1	0.121

# 3.2 Microstructure of as-cast and heat-treated alloys

Fig.3 shows the OM images of the as-cast and heat-treated alloys. The as-cast alloy exhibited two distinct  $\alpha$ -Al phases with differing morphologies: the primary  $\alpha$ 1-Al phase solidified in the shot sleeve, while the secondary  $\alpha$ 2-Al phase nucleated and grew within the die cavity. The  $\alpha$ 2-Al phase exhibited a much finer grain structure than  $\alpha$ 1-Al, due to the higher cooling rate achieved in the die cavity. Additionally, dendritic  $\alpha$ -Al structures along with fibrous eutectic Si (dark gray) and IMCs (light gray) were identified as the common microstructural features in the alloys. To better distinguish the contrast of different phases, the BSE images are shown in Fig.4. Six and five well-defined

areas with characteristic phases were detected in the BSE images of the as-cast and heat-treated alloys, respectively, through morphological analysis, contrast variation, and corroborating SEM-EDS data (Table 2). Region 1 exhibits dark grey cellular morphology, which is determined as α-Al phase. Region 2 displays an acicular shape and is confirmed as the Q-phase. The coarse blocky white phase and light gray eutectic phase are identified as Al<sub>2</sub>Cu phase (Region 3) and eutectic Si phase (Region 4), respectively. Additionally, the Mg-Si-rich dark region corresponds to Mg<sub>2</sub>Si phase (Region 5). Finally, the bright white phase which is not present in the heat-treated phase is identified as MgZn<sub>2</sub> phase (Region 6). Therefore, the heat treatment dissolves

all MgZn<sub>2</sub> phases into the matrix without altering the types of phases present. Fig. 5 presents the detailed microstructure and corresponding EDS maps of the alloys investigated. Notably, the Mg- and Zn-rich regions were eliminated following the heat treatment. Furthermore, after heat treatment, the volume fraction of the secondary phase decreases due to its dissolution into

the matrix (Table 3). During heat treatment, Si, Mg, and Cu in Al alloys are partially depleted from the solid solution (matrix) as they combine to form strengthening precipitates, leading to lower solute concentrations than in the as-cast state.

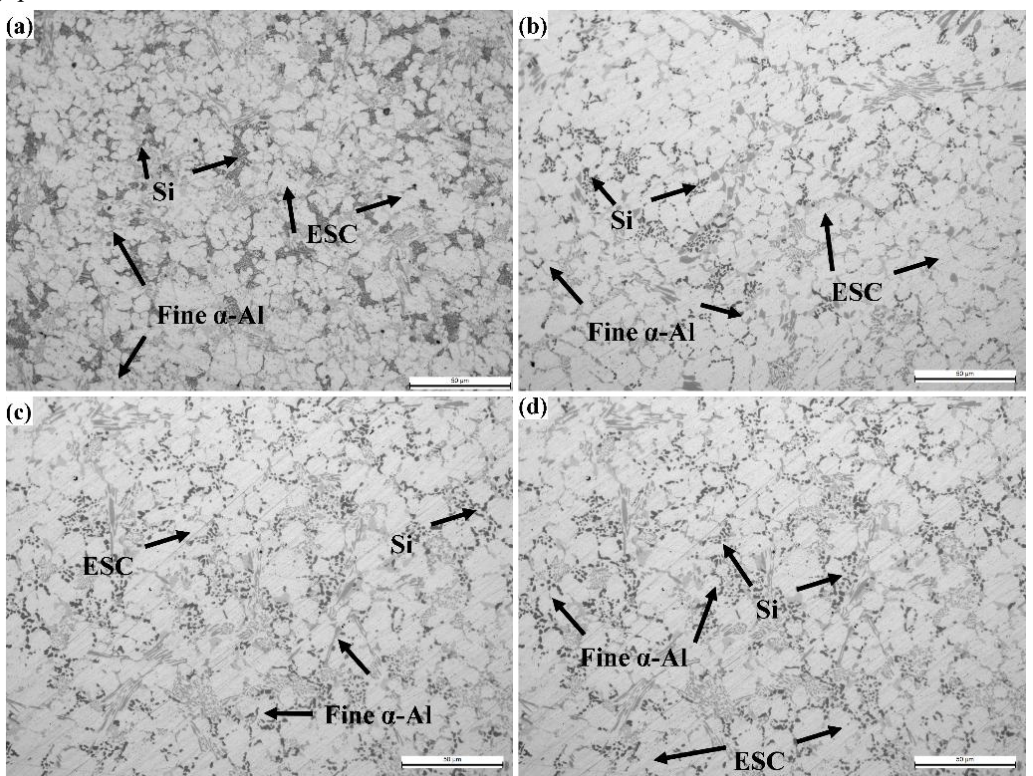


Fig.3: OM images of (a) as-cast alloy; (b)  $450^{\circ}$ C -0.5 h alloy; (c)  $450^{\circ}$ C -1 h alloy; (d)  $450^{\circ}$ C -2 h alloy

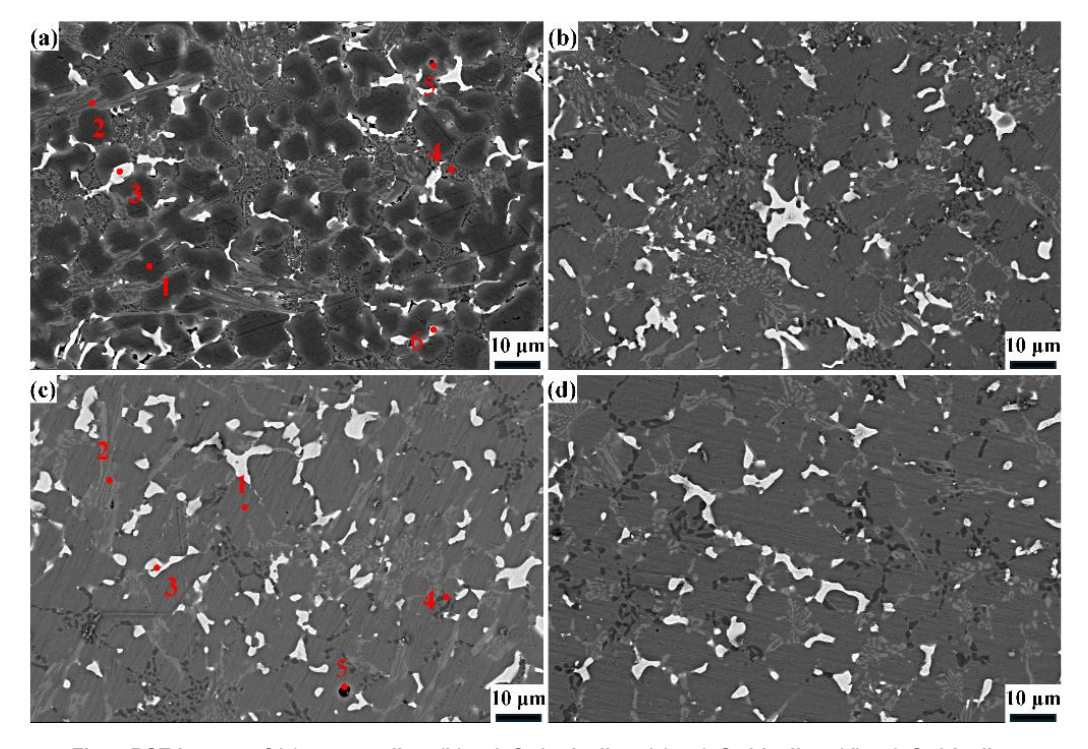


Fig.4: BSE images of (a) as-cast alloy; (b)  $450^{\circ}$ C -0.5 h alloy; (c)  $450^{\circ}$ C -1 h alloy; (d)  $450^{\circ}$ C -2 h alloy

	Table 3. Phase types, fract	ons, and compos	sitions in corresponding	a microstructure regions	s of the as-cast and 450°C-1 h alloys
--	-----------------------------	-----------------	--------------------------	--------------------------	---------------------------------------

A 11 a	Regions	Phase types	Volume fractions, %	Chemical compositions, at. %				
Alloys				Al	Si	Mg	Cu	Zn
	1	α-Al	76.96	94.55	1.23	1.26	0.84	2.12
	2	Q	10.34	41.43	21.03	27.22	7.74	2.58
A4	3	Al <sub>2</sub> Cu	10.02	69.10	1.23	0.88	27.11	1.68
As-cast	4	Si	2.25	41.29	55.95	0.64	1.29	1.83
	5	Mg <sub>2</sub> Si	0.19	47.09	17.63	30.56	1.83	2.89
	6	MgZn <sub>2</sub>	0.24	55.28	1.08	15.21	1.26	27.17
	1	α-Al	78.99	90.71	1.23	2.21	2.12	3.63
450°C-1 h	2	Q	9.42	45.27	17.82	19.52	15.17	2.22
	3	Al <sub>2</sub> Cu	8.19	68.00	1.24	2.32	26.72	1.72
	4	Si	1.91	33.27	63.12	1.42	0.93	1.26
	5	Mg <sub>2</sub> Si	1.49	53.46	15.12	27.12	1.61	2.69

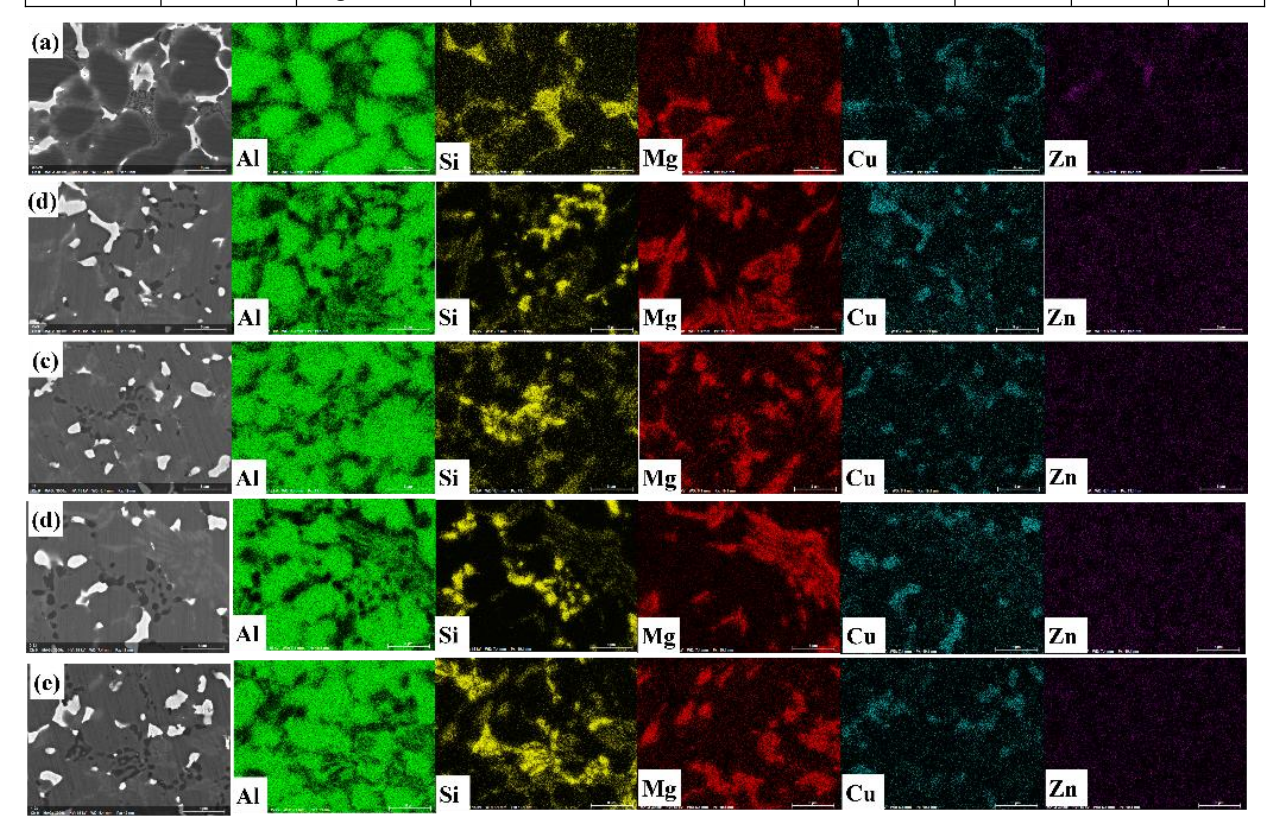


Fig.5: BSE images and corresponding EDS maps of (a) as-cast alloy; (b) 450°C -0.5 h alloy; (c) 450°C -1 h alloy; (d) 450°C -2 h alloy; (e) 450°C -3 h alloy

Fig. 6 presents the TEM analysis of the as-cast and  $450^{\circ}\text{C-1h}$  alloy. In the as-cast condition, nanoscale Mg-and Zn-rich precipitates were detected within the Al matrix, exhibiting alignment along the <001> Al direction (Fig.6(a) and (c)). Based on the SAED result, the precipitates are determined as  $\eta$  phase. In addition, there are some stacking faults and twins in the eutectics Si phase. The rapid solidification within the die cavity suppresses the growth of  $\{111\}_{\text{Si}}$  planes, resulting in the

generation of numerous stacking faults within eutectic Si particles. Si twinning occurs on  $\{111\}_{Si}$  planes with growth proceeding along the  $<112>_{Si}$  direction (indicated by black solid arrow). The  $70.5^{\circ}$  angle between twin planes confirms that the edge growth of Si strictly follows the twin plane re-entrant edge (TPRE) mechanism [28]. The TPRE, situated at the solidification front, serves as a preferential growth site for Si atoms, promoting rapid dendritic branching of Si particles along

the <112> crystallographic direction.

Additionally, in the  $450^{\circ}\text{C-1}$  h alloy, numerous precipitates with reticulated, vermicular, and globular morphologies are distributed throughout the matrix (Fig.6(d)). Si and Cu are highly concentrated in the reticulated, vermicular, and globular phases (Fig.6(e)). HRTEM images and corresponding FFT patterns confirm the presence of  $\beta''$ ,  $\theta'$ ,  $\eta'$  and Si phase in the Al matrix. The  $\beta''$  phase maintains full coherency with the matrix, whereas  $\theta'$  and  $\eta'$  phases exhibit semi-coherency. The spots in the FFT reveal the following orientation

relationships between the precipitates  $(\beta''/\theta'/\eta')$  and the Al matrix:  $(230)_{Al}//(100)_{\beta''}$  and  $[001]_{Al}$  //[010]  $_{\beta''}$ ,  $(001)_{Al}//(001)_{\theta'}$  and  $[100]_{Al}//[100]_{\theta'}$ ,  $[\bar{1}2\bar{1}3]_{\eta'}$ //[112]<sub>Al</sub> and  $(1\bar{2}12)_{\eta'}$  //(11 $\bar{1}$ )<sub>Al</sub>, respectively. These findings align with previous studies <sup>[29-31]</sup>. When the applied stress is below a critical level, these coherent or semi-coherent precipitates are usually cut by gliding dislocations, thereby hindering dislocation motion. Moreover, the Si phase lacks coherency with the matrix. These incoherent Si nanoparticles can induce dislocation pile-ups, leading to a strengthening effect.

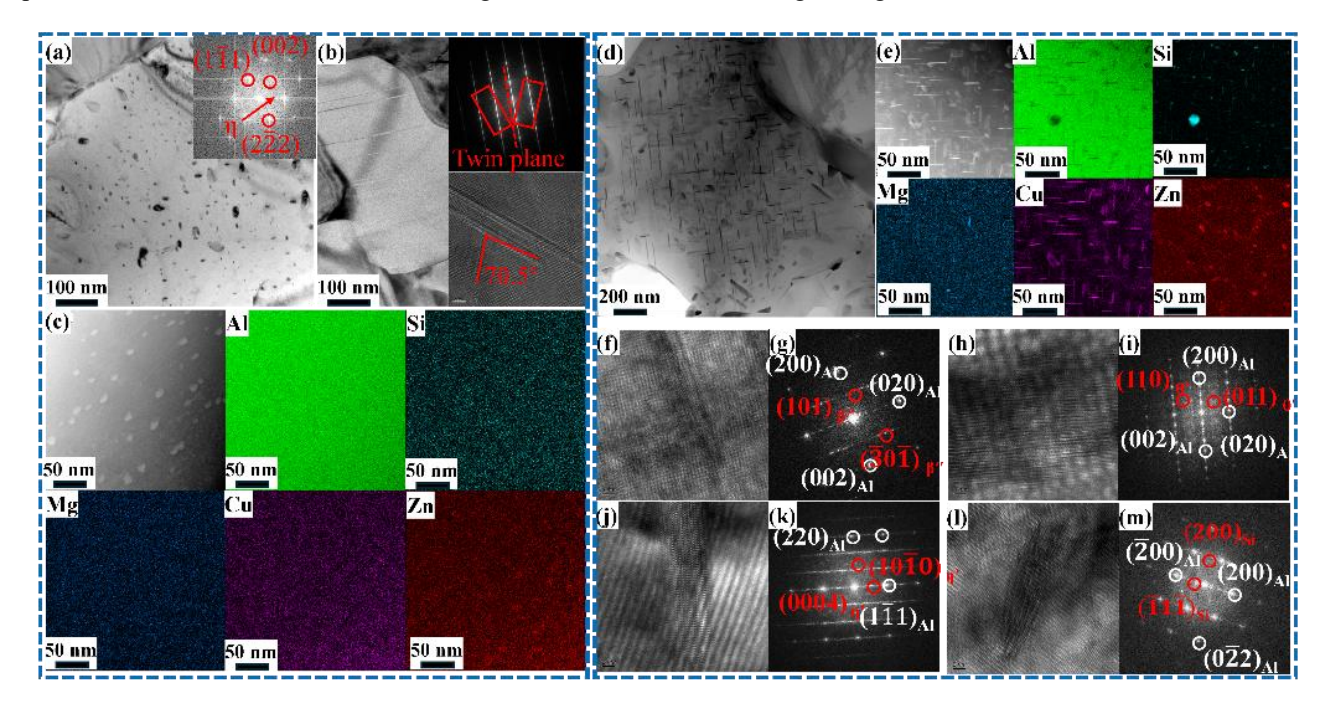


Fig.6: TEM analysis of the as-cast and 450°C -1 h alloy: the BF-TEM images of (a) precipitates, and (b) eutectics Si in the Al matrix in the as-cast alloy; (c) corresponding EDS maps in (a); (d) BF-TEM images of the 450°C -1 h alloy; (e) corresponding EDS maps in (d); HRTEM images and FFT patterns of β" (f) & (g), θ' (h) & (i), η' (j) & (k), and Si phase (l) & (m)

Fig.7 shows the 3D morphologies of IMCs in the as-cast and 450°C-1 h alloy. The volume fraction  $(V_f)$ , equivalent diameter  $(D_{eq} = \sqrt[3]{6V/\pi})$ , interconnectivity  $(I = V_{larg}/V)$ , and maximum volume  $(V_{max})$  were used to quantify the size and morphology of the IMCs. The equivalent diameter, denoted as  $D_{eq}$ , refers to the average diameter of particles within a given phase, accounting for variations in both their size and volume. I is defined as the ratio of the largest 3D individual volume  $(V_{larg})$  to the total volume (V) [32]. It should be noted that the different colors in the 3D visualization correspond to an independent phase. The outcomes of these parameters are presented in Table 4. The as-cast alloy contains 10.24% Q phase and 10.68% Al<sub>2</sub>Cu phase by volume. Following heat treatment, the volume fractions of the Q phase and Al<sub>2</sub>Cu phase were reduced by 9.09% and 20.32%, respectively. The maximum volume of Q phase was reduced from 8686.66 μm<sup>3</sup> to 7832.42 μm<sup>3</sup>, whereas the maximum volume of Al<sub>2</sub>Cu phase decreased significantly from 7211.25 µm<sup>3</sup> to 2049.22 µm<sup>3</sup> after heat treatment. Not surprisingly, the interconnectivity of Al<sub>2</sub>Cu phase dropped remarkably from 88.32% to 27.29%, which indicates that most of Al<sub>2</sub>Cu phases were fragmented during heat treatment. However, the interconnectivity of Q phase shows no obvious change. In addition, the equivalent diameter of Q phase and Al<sub>2</sub>Cu phase decreased by 10.24% and 14.60%, respectively, after heat treatment. The interconnectivity and maximum volume fraction of the Al<sub>2</sub>Cu phase exhibits a more pronounced reduction. This behavior is inherently linked to its higher solubility, accelerated coarsening kinetics during heat treatment, competitive interactions with other precipitates [33]. In contrast, the Q phase benefits from the synergistic effects of its multi-component composition and higher phase

stability, resulting in better retention of interconnectivity.

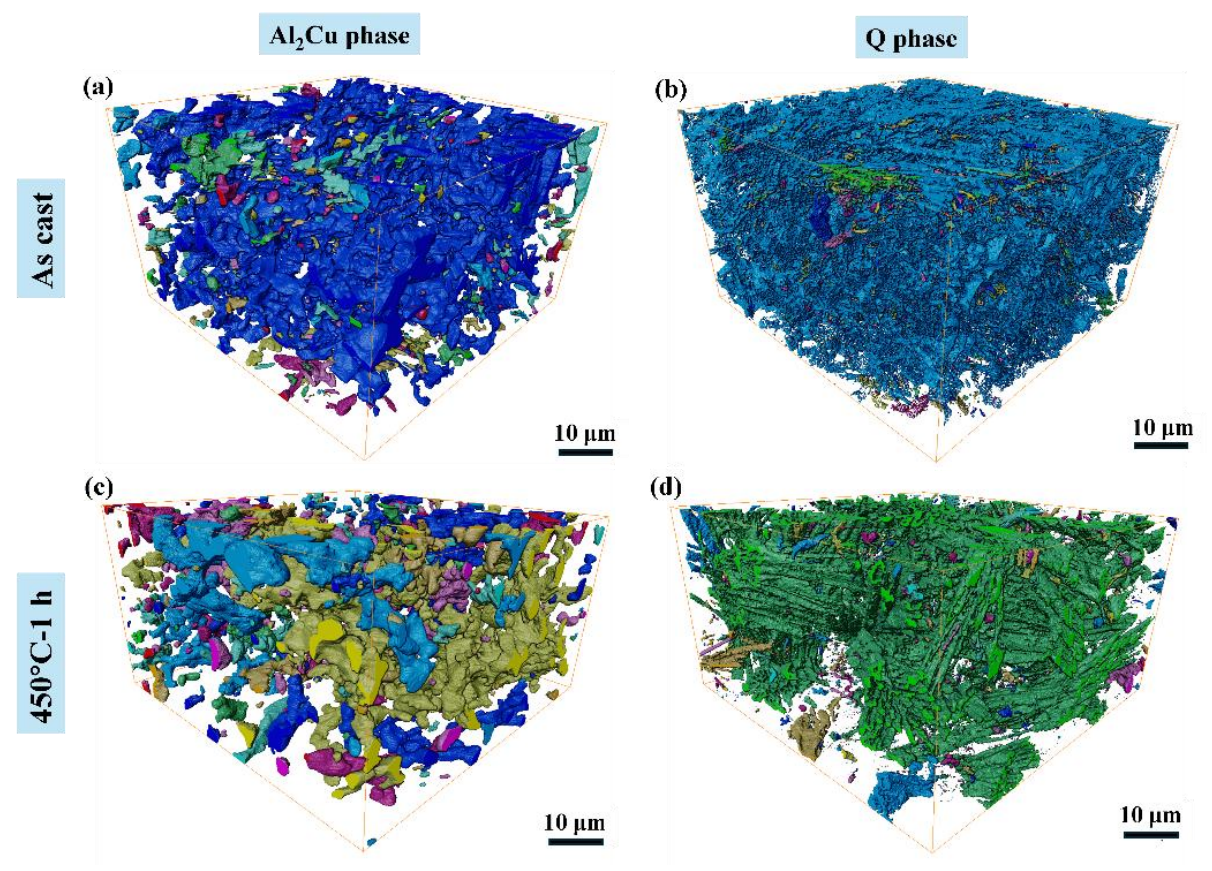


Fig.7: 3D morphologies of (a) Al2Cu phase and (b) Q phase in the as-cast alloy; (c) Al2Cu phase and (d) Q phase in the 450°C -1 h alloy

Table 4. Quantitative analysis of IMCs in the as-cast and 450°C-1h alloy

	Alloys	Q	Al <sub>2</sub> Cu
Volume fraction V (%)	As-cast	10.24	10.68
Volume fraction $V_f$ (%)	450°C-1 h	9.31	8.51
International I (0/)	As-cast	98.54	88.32
Interconnectivity I (%)	450°C-1 h	95.21	27.29
Equivalent diameter D (um)	As-cast	2.83	3.22
Equivalent diameter $D_{eq}$ ( $\mu$ m)	450°C-1 h	2.54	2.75
Mi	As-cast	8686.66	7211.25
Maximum volume $V_{max}$ ( $\mu$ m <sup>3</sup> )	450°C-1 h	7832.42	2049.22

# 3.3 Mechanical property and fracture behavior of the Al<sub>80</sub>Si<sub>8</sub>Mg<sub>4</sub>Cu<sub>4</sub>Zn<sub>4</sub> alloys

Fig.8 shows the compressive and tensile stress-strain curves of the as-cast and heat-treated alloys at 25 and 300°C. The compressive and tensile properties of the experimental alloys are presented in Fig.9. The 450°C-1 h alloy demonstrates optimal compressive and tensile performance under room-temperature conditions. The compressive strength and yield strength reaches 919 MPa and 566 MPa, respectively, with a fracture strain of 27.0%. This is mainly due to the improved solid solution strengthening from Mg, Si, Zn, and Cu atoms, as well as

possible precipitation strengthening by  $\beta''$ ,  $\theta'$ , and  $\eta'$  phases. For tensile strength, the 450°C-1 h alloy achieves an ultimate tensile strength of 376 MPa and an elongation of 1.55%. With prolonged solution treatment, the compressive strength and ultimate tensile strength progressively decreased, reaching 900 MPa and 373 MPa after 2 h and 896 MPa and 368 MPa after 3 h. Meanwhile, the fracture strain and elongation increase after heat treatment, and decrease gradually with increasing solution time from 1 h to 3 h. The increase in fracture strain and elongation observed after solution treatment are mainly due to grain coarsening and spheroidization of

the secondary phases. As shown in Fig. 10, the solution treatment significantly reduced both the crack density and crack length. Furthermore, Fig.11 shows the tensile fracture morphologies of experimental alloys. After heat treatment, the increase of tear ridges and decrease of cleavage plane on the fractured surface indicates

improved plasticity. And the decreased fracture strain and elongation as the solid solution time increases are associated with the coarsening of secondary phase. The coarse secondary phases act as stress concentration points, promoting crack initiation and thereby decreasing plasticity.

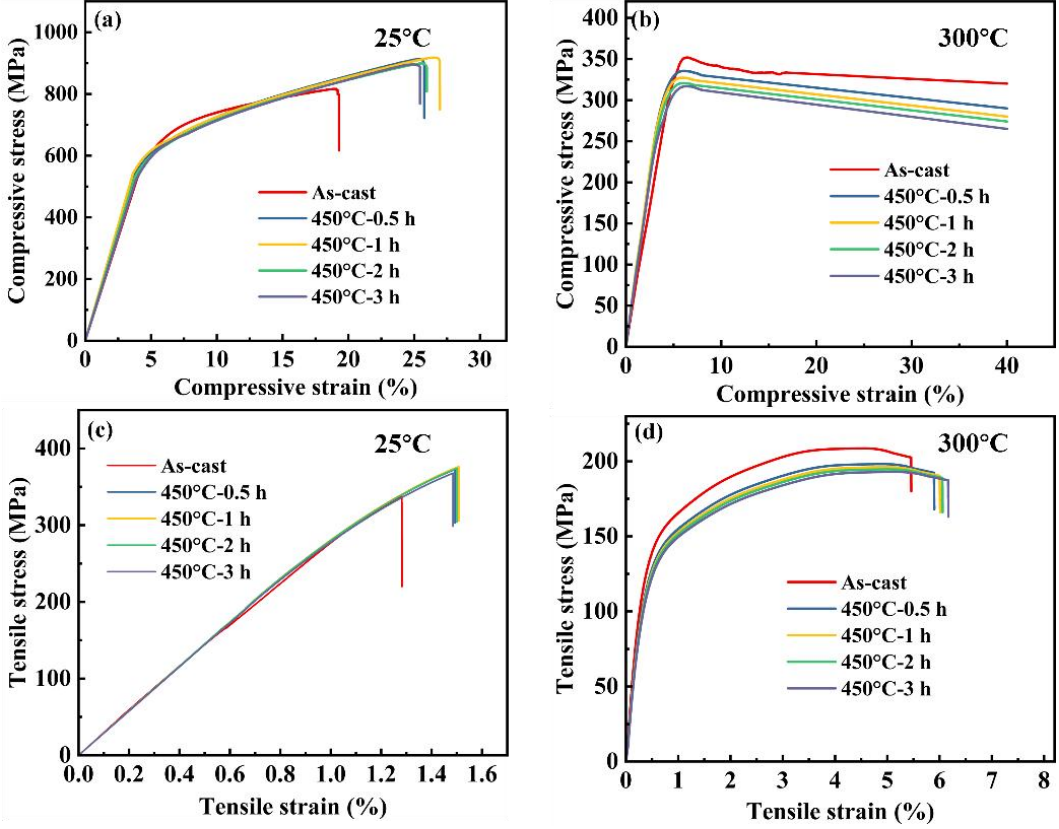


Fig.8: Compressive stress-strain curves of the as-cast and heat-treated alloys at (a) 25°C, and (b) 300°C; tensile stress-strain curves of the as-cast and heat-treated alloys at (a) 25°C, and (b) 300°C.

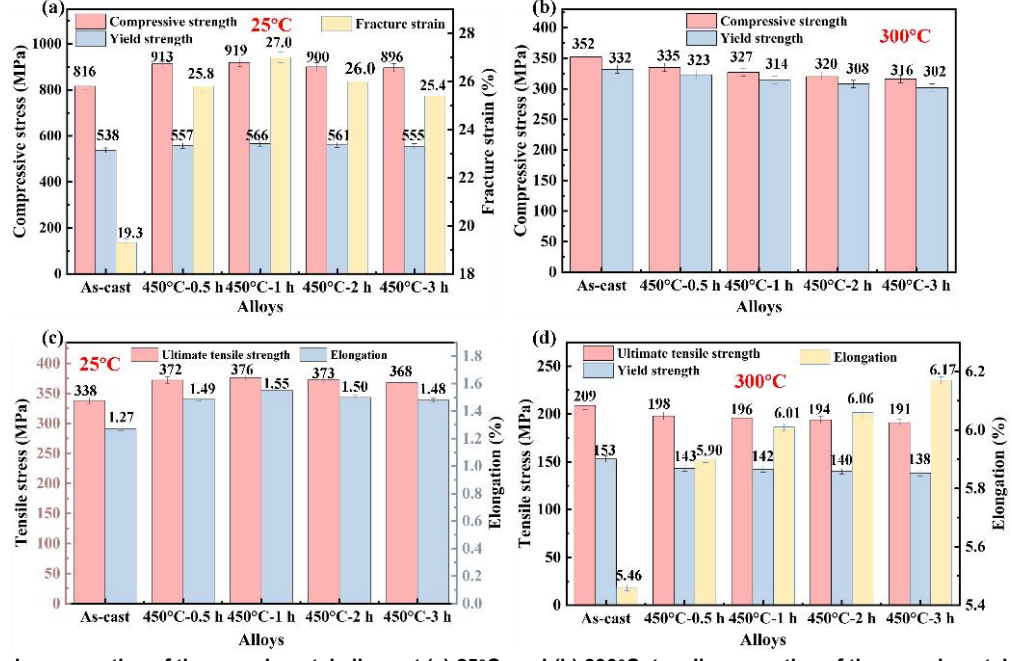


Fig.9: Compressive properties of the experimental alloys at (a) 25°C, and (b) 300°C; tensile properties of the experimental alloys at (c) 25°C, and (d) 300°C

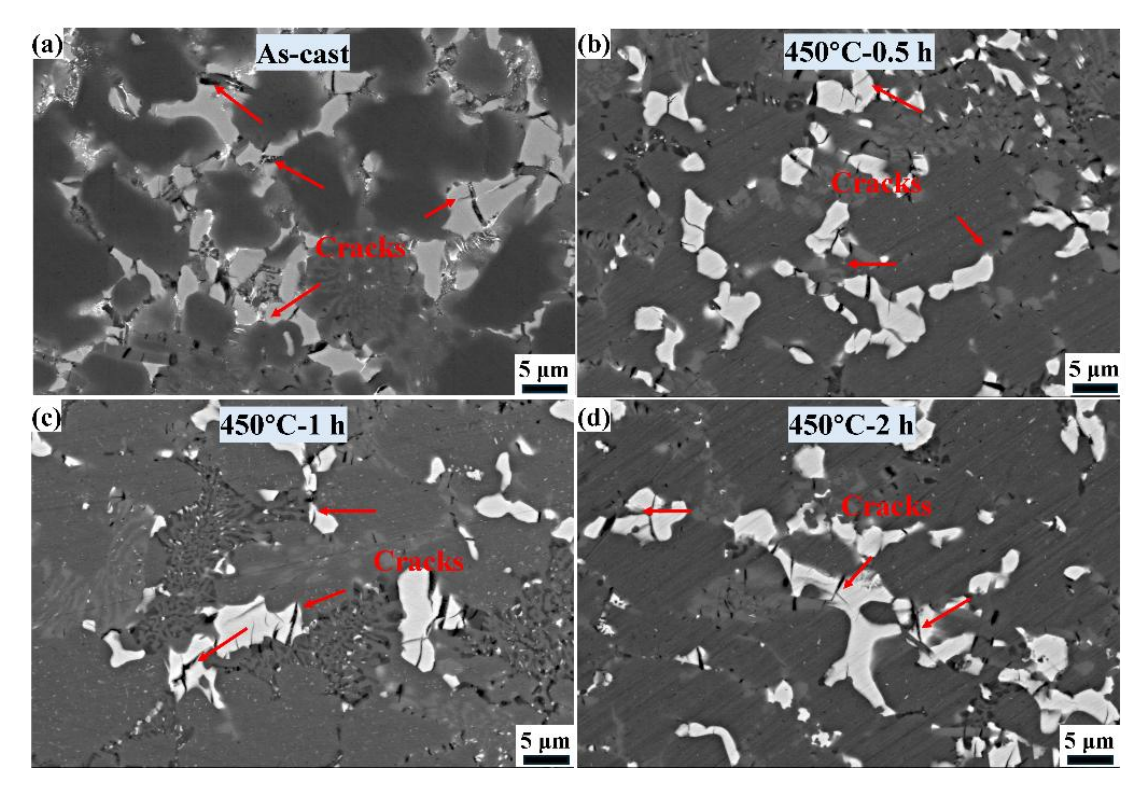


Fig.10: BSE images of compressive fracture specimens at 25°C: (a) As-cast alloy; (b) 450°C-0.5 h alloy; (c) 450°C-1 h alloy; (d) 450°C-2 h alloy

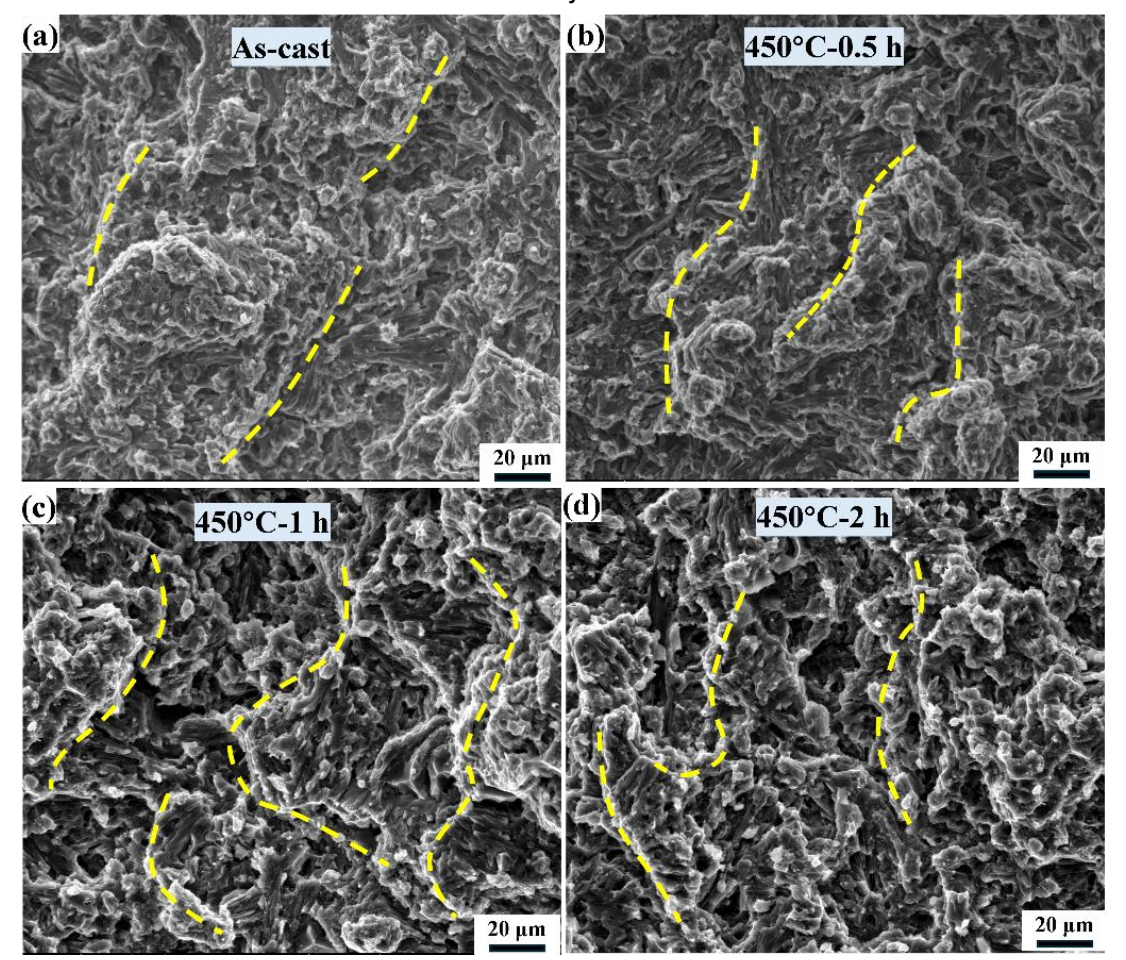


Fig.11: Tensile fracture morphologies at 25°C of: (a) As-cast alloy; (b) 450°C-0.5 h alloy; (c) 450°C-1 h alloy; (d) 450°C-2 h alloy

At 300°C, the as-cast alloy exhibits the highest compressive and tensile strength among all alloys. The compressive strength drops from 352 MPa to 316 MPa, while the ultimate tensile strength declines from 209 MPa to 191 MPa, with an extension of the solution time. The tensile and compressive yield strength also decreases after heat treatment. Moreover, the heat-treated alloys exhibit greater elongation compared to the as-cast alloy. After aging treatment, although the room-temperature strength is improved, the precipitates become unstable at elevated temperatures, resulting elevated-temperature strength compared to the as-cast state. Furthermore, at elevated temperatures, as the Al matrix softens, its interconnected network structure is crucial for transferring external loads from the ductile Al matrix to the rigid secondary phases, significantly affecting the alloy's mechanical properties [34]. Consequently, due to the disruption of the rigid phase network structures during heat treatment (Fig.7), the alloy's strength declines at elevated temperatures.

Fig.12 shows the TEM results after compression at 300°C. The matrix contains numerous precipitates and dislocations. Dislocations become entangled around the effective precipitates, indicating strengthening (Fig.12(a)). The dislocations and twins in the Si phase become more densely distributed. In addition, many nano-Al<sub>2</sub>Cu phases appear in the Si phase, which were identified by SAED. Nano-scale coherent Al<sub>2</sub>Cu particles are key strengthening contributors, as they anchor dislocations and restrict their movement. Stacking faults and twins also significantly hinder dislocation slip, with their combined interactions amplifying the strengthening mechanism [35]. According to EDS maps, dislocation accumulation occurs near Al<sub>2</sub>Cu and O-phase regions, resulting in the cracking of these phases.

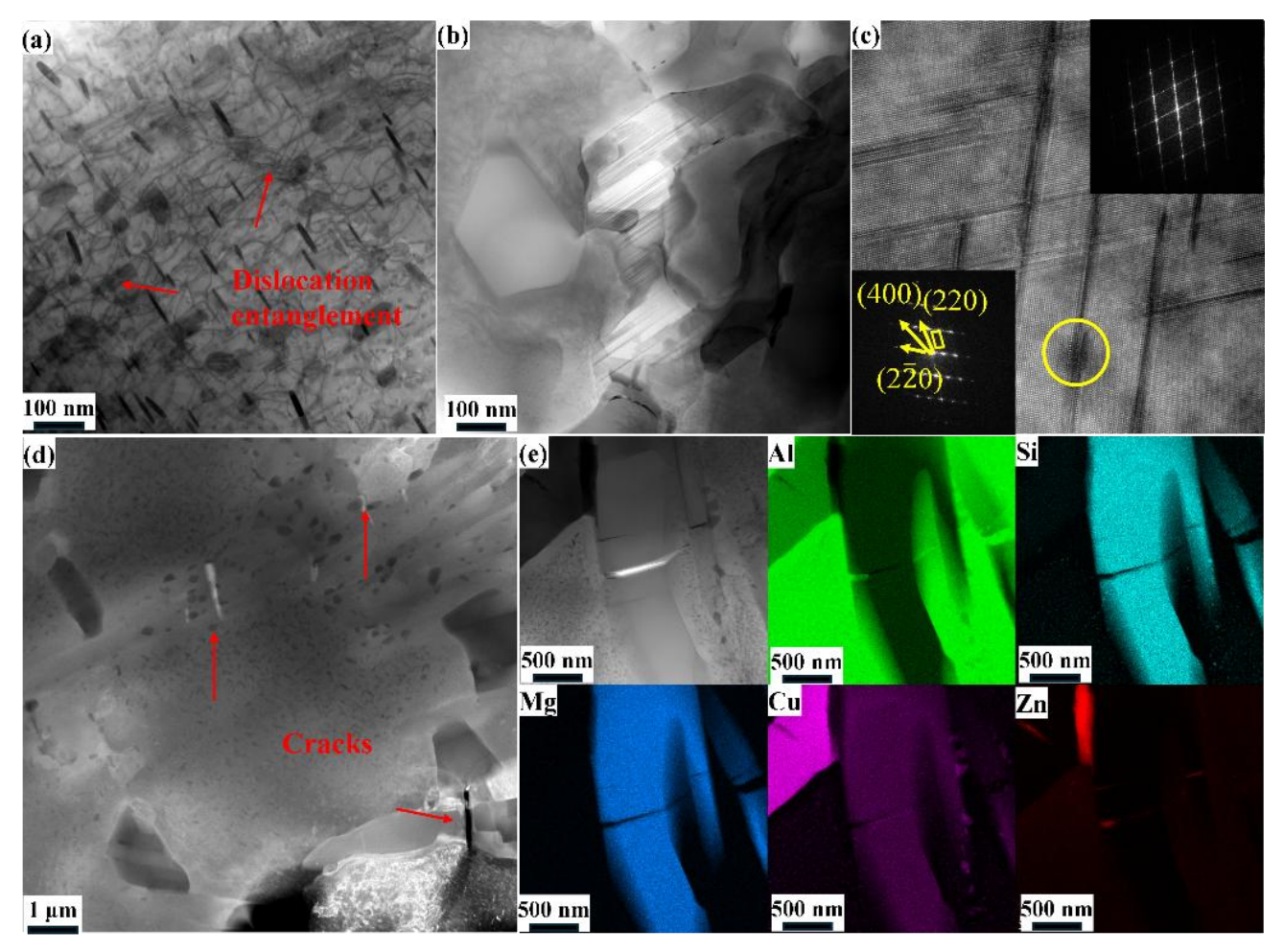


Fig.12: TEM results after compression at 300°C of as-cast alloy: (a) BF-TEM image of precipitates and dislocations; (b) BF-TEM image and (c) HR-TEM image of Si phase; (d) BF-TEM image of IMCs and (e) corresponding EDS maps.

Fig. 13 compares the yield strength of the as-cast alloy with commercial industrial Al alloys at both room and elevated temperatures. The as-cast alloy

demonstrates significantly enhanced performance over conventional high-performance Al alloys, underscoring its strong potential for high-temperature applications.

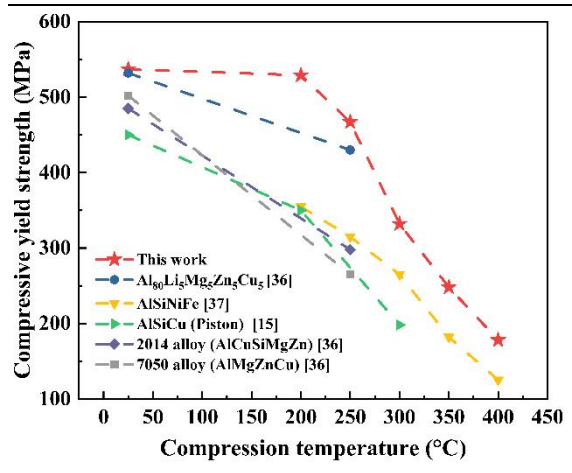


Fig.13: Comparison of yield strength vs. compression temperature for as-cast alloy and other industrial high-strength Al alloys [15, 36, 37]

#### **4 Conclusions**

In this study, a novel Al<sub>80</sub>Si<sub>8</sub>Mg<sub>4</sub>Cu<sub>4</sub>Zn<sub>4</sub> alloy was successfully produced by industrial vacuum-assisted die casting, the effects of heat treatment on the microstructure and mechanical performances at room and elevated temperatures were further investigated. The main conclusions are as follows:

- (1) The as-cast  $Al_{80}Si_8Mg_4Cu_4Zn_4$  alloy consisted of  $\alpha$ -Al, Q,  $Al_2Cu$ , eutectic Si,  $Mg_2Si$  and  $MgZn_2$  phases, which aligned well with the calculation results.
- (2) After heat treatment, MgZn<sub>2</sub> phase completely dissolved in the Al matrix. Coherent and semi-coherent β", θ', and η' phases formed within the Al matrix, resulting in precipitation strengthening. Moreover, the interconnectivity of Al<sub>2</sub>Cu phase decreased from 88.32% to 27.29%. Meanwhile, the Q phase experienced minimal shifts in interconnectivity.
- (3) The 450°C-1 h alloy showed superior mechanical performance at room temperature. This is mainly attributed to the high-density nano precipitates in the Al matrix, as well as numerous stacking faults and twins in the Si phase.
- (4) The as-cast alloy exhibited outstanding mechanical performance at elevated temperatures than other industrial high-performance Al alloys, which shows great potential for applications at elevated temperatures. This is mainly due to the highly interconnected network of IMCs and nano-precipitates in the Al matrix.

# Acknowledgments

The research was financially supported by Beijing

Natural Science Foundation-Millet Innovation Joint Fund (No. L223001), Natural Science Foundation of Guangdong Province (No. 2023A1515012730) and the Key Area Research and Development Program of Guangdong Province (No. 2020B010186002).

# **Conflicts of interest**

The authors declare that they have no known competing financial interests or personal relationships that could have appeared to influence the work reported in this paper.

# References

- [1] Dong J, Jiang J, Wang Y, et al. Effect of casting process and Zr, V addition on microstructure and mechanical properties of Al–12Si-4.5Cu–2Ni alloy [J]. Journal of Materials Research and Technology, 2024, 29: 1428-40.
- [2] Hirsch J. Recent development in aluminium for automotive applications [J]. Transactions of Nonferrous Metals Society of China, 2014, 24(7): 1995-2002.
- [3] Asadikiya M, Yang S, Zhang Y, et al. A review of the design of high-entropy aluminum alloys: a pathway for novel Al alloys [J]. Journal of Materials Science, 2021, 56(21): 12093-110.
- [4] Asadikiya M, Zhang Y, Wang L, et al. Design of ternary high-entropy aluminum alloys (HEAls) [J]. Journal of Alloys and Compounds, 2022, 891.
- [5] Xiong W, Guo A X Y, Zhan S, et al. Refractory high-entropy alloys: A focused review of preparation methods and properties [J]. Journal of Materials Science & Technology, 2023, 142: 196-215.
- [6] Guo B, Cui D, Wu Q, et al. Segregation-dislocation self-organized structures ductilize a work-hardened medium entropy alloy [J]. Nature Communications, 2025, 16(1): 1475.
- [7] Li R X, Geng G H, Zhang Y. Recent progress in lightweight high-entropy alloys [J]. MRS Communications, 2023, 13(5): 740-53.
- [8] Liao Y C, Li T H, Tsai P H, et al. Designing novel lightweight, high-strength and high-plasticity Ti (AlCrNb)100- medium-entropy alloys [J]. Intermetallics, 2020, 117.
- [9] Feng R, Gao M C, Zhang C, et al. Phase stability and transformation in a light-weight high-entropy alloy [J]. Acta Materialia, 2018, 146: 280-93.
- [10] Wen J C, Cheng J H, Min X D, et al. Strengthened solid solution and homogenized eutectic structure of Al-based multi-component alloy via electromagnetic stirring [J]. Journal of Alloys and Compounds, 2024, 1002: 175537.
- [11] Cui L Y, Zhang Z, Chen X G. Lightweight Al-based

- entropy alloys: Overview and future trend [J]. Science China Materials, 2023, 67(1): 31-46.
- [12] Ahn T-Y, Jung J-G, Baek E-J, et al. Temporal evolution of precipitates in multicomponent Al–6Mg–9Si–10Cu–10Zn–3Ni alloy studied by complementary experimental methods [J]. Journal of Alloys and Compounds, 2017, 701: 660-8.
- [13] Han M J, Wu Y, Zong X B, et al. Lightweight single-phase Al-based complex concentrated alloy with high specific strength [J]. Nature Communications, 2024, 15(1): 7102.
- [14] Wen J C, Liu Y, Huang Y C, et al. Effects of electromagnetic stirring and subsequent homogenization treatment on the microstructure and mechanical properties of Al70Zn10Mg10Cu5Si5 multi-component alloy [J]. Journal of Alloys and Compounds, 2023, 960: 170725.
- [15] Baek E-J, Ahn T-Y, Jung J-G, et al. Effects of ultrasonic melt treatment and solution treatment on the microstructure and mechanical properties of low-density multicomponent Al70Mg10Si10Cu5Zn5 alloy [J]. Journal of Alloys and Compounds, 2017, 696: 450-9.
- [16] Gao M C, Yeh J-W, Liaw P K, et al. High-entropy alloys: fundamentals and applications [M]. Springer, 2016.
- [17] Tseng K, Yang Y, Juan C, et al. A light-weight high-entropy alloy Al 20 Be 20 Fe 10 Si 15 Ti 35 [J]. Science China Technological Sciences, 2018, 61: 184-8.
- [18] Qi M F, Kang Y L, Xu Y Z, et al. A novel rheological high pressure die-casting process for preparing large thin-walled Al–Si–Fe–Mg–Sr alloy with high heat conductivity, high plasticity and medium strength [J]. Materials Science and Engineering: A, 2020, 776.
- [19] Zhang Y X, Zhao H D, Liu F. Microstructure characteristics and mechanical properties improvement of gravity cast Al-7Si-0.4Mg alloys with Zr additions [J]. Materials Characterization, 2021, 176: 111117.
- [20] Zhao H-d, Wang X-l, Wan Q, et al. Characteristics and distribution of microstructures in high pressure die cast alloys with X-ray microtomography: A review [J]. China Foundry, 2024, 21(5): 427-44.
- [21] Pola A, Tocci M, Goodwin F E. Review of Microstructures and Properties of Zinc Alloys [J]. Metals, 2020, 10(2).
- [22] Liu F, Qin J, Zhao H D, et al. Influence of intermetallics and element concentrations on the performance of the heat treated HVDC AlSiMgMnCu alloys at nano-scale [J]. Materials & Design, 2023, 229: 111902.
- [23] Wang X L, Zhao H D, Xu Q Y, et al. Clustering characteristics of Fe-rich intermetallics in high

- vacuum die cast AlSiMgMn alloys with high resolution  $\mu$ -CT inspection [J]. Materials Characterization, 2024, 207: 113607.
- [24] Liu F, Zheng H T, Zhong Y, et al. Effect of Cu/Mg-containing intermetallics on the mechanical properties of the as-cast HVDC AlSiMgMnCu alloys by SBFSEM at nano-scale [J]. Journal of Alloys and Compounds, 2022, 926: 166837.
- [25] Miracle D B, Senkov O N. A critical review of high entropy alloys and related concepts [J]. Acta Materialia, 2017, 122: 448-511.
- [26] Yang X, Zhang Y. Prediction of high-entropy stabilized solid-solution in multi-component alloys [J]. Materials Chemistry and Physics, 2012, 132(2-3): 233-8.
- [27] Heydari H, Tajally M, Habibolahzadeh A. Calculations to introduce some light high entropy alloys based on phase formation rules [J]. Journal of Alloys and Compounds, 2022, 912.
- [28] Dong J, Jiang J, Wang Y, et al. Effect of Er, Zr, V, Ti microalloying and muti-field coupling melt deep purification on the microstructure and mechanical properties of Al-12Si-4.5Cu-2Ni alloy [J]. Materials Science and Engineering: A, 2025, 923.
- [29] Yang H L, Ji S X, Yang W C, et al. Effect of Mg level on the microstructure and mechanical properties of die-cast Al–Si–Cu alloys [J]. Materials Science and Engineering: A, 2015, 642: 340-50.
- [30] Kim Y-Y, Rosenthal D F T, Shin D, et al. Effects of Sn addition on precipitation of a pre-naturally aged Al–Zn–Mg alloy during artificial aging [J]. Materials Characterization, 2024, 207.
- [31] Kayani S H, Lee S-U, Euh K, et al. Effect of as-cast microstructure on precipitation behavior and thermal conductivity of T5-treated Al 7Si 0.35Mg alloy [J]. Journal of Alloys and Compounds, 2024, 976.
- [32] Liu F, Zhao H D, Chen B, et al. Investigation on microstructure heterogeneity of the HPDC AlSiMgMnCu alloy through 3D electron microscopy [J]. Materials & Design, 2022, 218: 110679.
- [33] Sjölander E, Seifeddine S. Optimisation of solution treatment of cast Al–Si–Cu alloys [J]. Materials & Design, 2010, 31: S44-S9.
- [34] Requena G, Garcés G, Asghar Z, et al. The Effect of the Connectivity of Rigid Phases on Strength of Al-Si Alloys [J]. Advanced Engineering Materials, 2011, 13(8): 674-84.
- [35] Shi Z, He R, Chen Y, et al. Microstructural evolution and strengthening mechanisms of a novel

Al-11Si-3Cu alloy microalloyed with minor contents of Sr and Sc [J]. Materials Science and Engineering: A, 2022, 853.

[36] Li H Z, Yang C, Fu J N, et al. Nano-amorphous—crystalline dual-phase design of Al80Li5Mg5Zn5Cu5 multicomponent alloy [J].

Science China Materials, 2022, 65(6): 1671-8.

[37] Cai Q, Fang C M, Lordan E, et al. A novel Al-Si-Ni-Fe near-eutectic alloy for elevated temperature applications [J]. Scripta Materialia, 2023, 237: 115707.